Inverted Honeycomb Cell as a Reinforcement Structure for Building Soft Pneumatic Linear Actuators

François Schmitt, Olivier Piccin, Pierre Renaud, Bernard Bayle, Laurent Barbé

Inverted Honeycomb Cell as a Reinforcement Structure for Building Soft Pneumatic Linear Actuators

François Schmitt
AVR – ICube,
CNRS,
University of Strasbourg,
Strasbourg 67081, France
e-mail: francois.schmitt@unistra.fr

Olivier Piccin
AVR – ICube,
CNRS,
INSA Strasbourg,
University of Strasbourg,
Strasbourg 67081, France
e-mail: olivier.piccin@insa-strasbourg.fr

Bernard Bayle
AVR – ICube,
CNRS,
University of Strasbourg,
Strasbourg 67081, France
e-mail: bernard.bayle@unistra.fr

Pierre Renaud
AVR – ICube,
CNRS,
INSA Strasbourg,
University of Strasbourg,
Strasbourg 67081, France
e-mail: pierre.renaud@insa-strasbourg.fr

Laurent Barbé
AVR – ICube,
CNRS,
University of Strasbourg,
Strasbourg 67081, France
e-mail: laurent.barbe@unistra.fr

In this article, the inverted honeycomb cell, known to exhibit an auxetic behavior, is considered to design two pneumatic linear actuators. The actuators are built using a combination of soft and rigid structures. They present complementary performances in terms of displacement, force and stiffness. Experimental evaluations are conducted using prototypes produced using multimaterial additive manufacturing to combine soft and rigid materials with freedom of shape. The first actuator is inspired by origami structures. The possibility to obtain large deformations under low pressure is observed. The second actuator is based on a cylindrical auxetic structure based on the inverted honeycomb cell. Smaller deformation is reached but the design favors the off-axis stiffness, so the component can be integrated without any additional mechanical joint for translation. A discussion on the relative performances of these two actuators and their possible uses concludes the paper.

1 Introduction

Since the early 2000's, soft robots have widespread to become a new field of exploration for researchers, somehow separated from the development of more classical rigid robots. Contrary to stiffer structures able to work at very high speed and accuracy levels, highly deformable components allow to create compact and lightweight devices that are still capable of delivering high power and can exhibit high intrinsic compliance. They are consequently particularly relevant for applications where safety and/or adaptability are major concerns, such as collaborative robots [1], exploration robots [2], surgical robots [3], or exoskeletons [4, 5].

Although the motion of soft robots is harder to model in comparison with their rigid counterparts, well characterized by rigid body kinematic models, several research groups have worked on the development of new actuators that could be used to produce elementary motions. Many actuation solutions have been proposed in the literature, including but not limited to thermo-activated materials such as shape-memory materials (metallic alloys [6–8] or polymers [9, 10]) or materials exploiting phase transition [11, 12], electro-active poly-

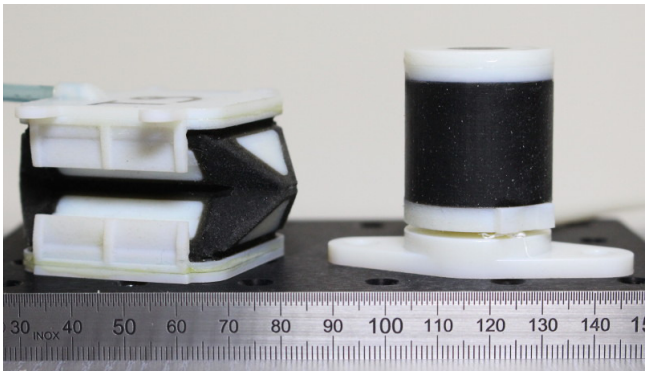

Fig. 1. Prototypes of proposed pneumatic soft linear actuators: (left) deployable origami-inspired actuator and (right) auxetic actuator.

mers [13, 14] or fluidic actuation [15–18]. Among these solutions, pneumatic actuators are of particular interest as they allow for a very high power density with a relatively fast response time if pneumatic distribution system and controller are carefully designed [19]. In order to limit the impact of distribution components on the bulk of the system, they can be deported from the actuation site at the cost of increased latency and modified dynamics of overall device.

Soft actuators have their body mainly composed of materials with low Young's modulus, typically a few GPa or less, following [20]. Soft pneumatic actuators are generally single stroke actuators that rely either on their intrinsic stiffness to return to their initial position [21,22] or on antagonistic setup with either a similar actuator or an additional elastic element to provide a spring effect [4, 23]. This elastic element can be designed using stiffening layers, such as fibrous matrices, or by thickening specific areas in order to create the required motion [24]. One of the most notable examples are McKibben muscles [25] that use inextensible fibers wound about a cylindrical room. As the room inflates, the fibers restrict the radial expansion of the "muscle", resulting in the contraction of the actuator [26–28]. These actuators, first developed in the 1950's, have since then been used in a wide range of applications. Similar concepts of bio-inspired contractile muscles have also been proposed, such as the pleated pneumatic artificial muscles [29] or buckling cellular networks that collapse under vacuum [22]. As those systems work in contraction they have a lower risk of buckling than extension actuators and are adapted to orthotics [4, 5] and bio-inspired mechanisms [23]. Soft pneumatic extension actuators are much less frequent, as their tendency to buckle usually limit their maximum length. In these actuators, radial expansion is restricted to favor the longitudinal expansion. This is commonly achieved by the addition of stiffening materials such as fibers [5] or stiffer elastomers [30, 31] or by locally stiffening the geometry [32]. The actuators are then designed to offer specific displacement and force characteristics. They do not generally offer resistance to loads in directions other than the actuator elongation, which means the actuator off-axis stiffness is not investigated during the design.

In the present work, the design of soft pneumatic extension actuators (shown in Fig. 1) is presented. Two designs are described and compared. They take advantage of the contrast between mechanical properties of a stiff polymer and a much softer elastomer (three orders of magnitude between their respective Young's modulus [33]) to combine several functions in a compact manner. The difference of stiffness between the materials leads us to describe the actuators as a combination of soft and rigid materials, to form hybrid soft/rigid actuators as designated in [34]. The actuators include a rigid reinforcement structure which design is inspired from the inverted honeycomb cell. From the cell geometry, the two actuators are built with complementary balance between in-axis compliance, force capability and also off-axis stiffness.

The design work is conducted having in mind applications in the medical field. Actuators need then to be of small size for integration in medical robots, and also possibly compatible with stringent requirements such as compatibility with medical imaging devices [35, 36]. This motivates the choice of actuator manufacturing with a particular type of additive manufacturing, Multi-Material Additive Manufacturing (MMAM), in order to combine easily soft and rigid polymer materials and try to maximize compactness.

This paper is organized as follows. In section 2, the design approach starting from the requirements and the interest of the inverted honeycomb cell is described. The principles adopted for the two actuators are then briefly presented. In sections 3 and 4, we go into the specific details of both designs, focusing more on their respective challenges and how they were tackled, including the manufacturing constraints. Then, in section 5, the experimental characterization carried out on both designs are presented, showing the performances of each actuator. Finally, section 6 describes the respective performance and interest of the two actuators and some possible fields of applications.

2 Inverted honeycomb cells for linear motion

2.1 Design objectives

Soft pneumatic actuators that are manufactured using only soft materials behave as balloons: when they are inflated using pressurized fluid, they expand in all directions. When such an actuator interacts with a load, most of the input power is used for the system deformation and not for the task itself. To generate a motion in a specific direction, soft pneumatic actuators are designed with a reinforcement structure. Up to now, the actuators suffer however from a limited kinematic accuracy, as the reinforcement is designed to control the motion, but not the resistance to forces applied in other directions. When accuracy is needed, an external stiffer structure or "skeleton" has to be added [23]. We consider in this paper the integration of this skeleton as an intrinsic part of the actuator. It acts both as a reinforcement to guide the motion in one direction, and also helps withstanding transverse forces. This combination of soft elements with a stiffer structure creates the actuators. The goal is to have actuators offering a customizable trade-off between the following de-

sign properties:

Off-axis stiffness: withstanding external transverse forces helps guiding the motion and limits a potential drift in the motion axis position and orientation. This allows predicting more easily the behavior of the actuator by using for example pseudo-rigid body models [37].

In-axis compliance: the use of pneumatic energy and soft materials allows such actuators to be compressible. This means that the actuator can act as a security component and limit interaction forces.

Force capability: conversely, the inclusion of some rigid elements in the design would allow increasing the pressure level. Consequently, if higher forces are required, they can be generated by such an actuator.

Compactness: enclosing both the actuation and the guiding structure in the same design allows reducing the bulk by integrating several function in the same system.

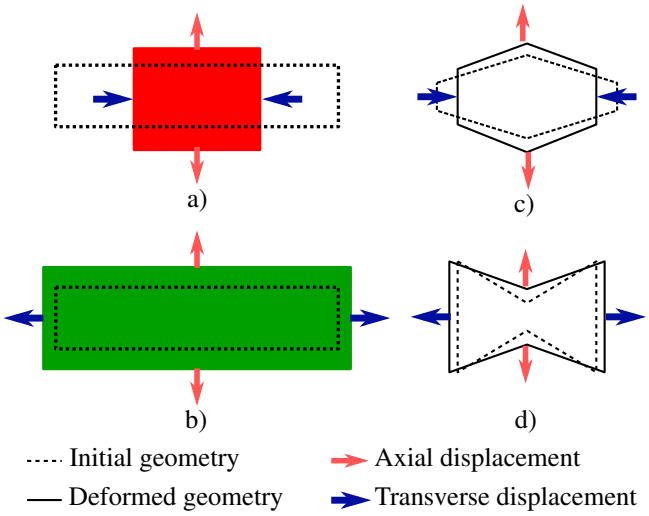

Fig. 2. a) Material with positive Poisson's ratio and b) material with negative Poisson's ratio. The honeycomb (c) and inverted honeycomb (d) cells before and after deformation. The relationship between axial and radial displacement differ between the two cells.

For the reinforcement structure, our proposition in this paper is to exploit the inverted honeycomb cell to adjust these four characteristics. The cell is represented in Fig. 2. Fig. 2a) and c) show a material made with classical honeycomb cell with a positive Poisson's ratio. A radial compression induces an axial expansion. In contrary, the material made with inverted honeycomb cell has an auxetic behavior with a negative Poisson's ratio (Fig. 2b) and d)). In other words, a radial expansion induces an axial expansion.

2.2 A deployable pocket actuator

A first way to design an actuator from the inverted honeycomb cell is to get inspiration from cellular actuators [38, 39] and origami designs [40, 41]. The proposition is then to use the inverted honeycomb cell as an articulated

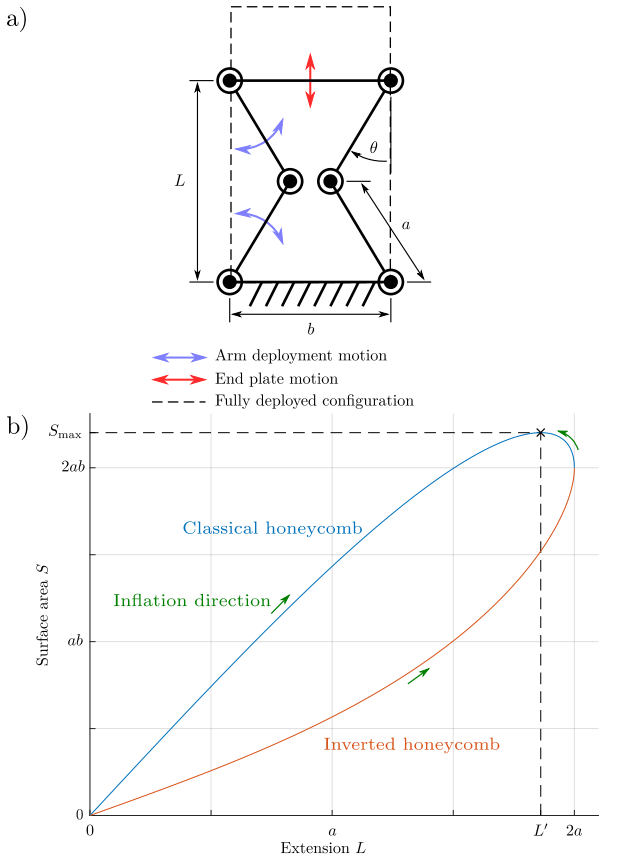

Fig. 3. Illustration of the honeycomb cell as a deployable tube section. a) Presentation of the pattern and its parameters. b) Evolution of the internal surface area S with respect to the extension L in both classical and inverted honeycomb patterns, with $b = 2a$. The simulation shows that the maximum of surface area $S_{\max}$ is not reached for the maximum extension $L = 2a$, limiting the maximum reachable extension of the classical honeycomb cell to a value $L' < 2a$.

mechanism composed of rigid links as described in Fig. 3a). The increase under pressure of the internal volume delimited by the articulated structure is then used to get the actuator motion. This shape guarantees a monotonic increase of the internal volume during the structure deployment, as presented in the following. More specifically, it permits a full deployment of the pattern unlike the classical honeycomb shape (see Fig. 3b)). Consequently, a design based on an inverted honeycomb cell will be more compact for a same displacement range. The actuator will be designated in the following as a deployable pocket actuator and will be presented in section 3.

2.3 An auxetic reinforced actuator

Another way to design an actuator is to create a pattern of cells, and build the actuator as a simple soft tubular actuator reinforced by this structure, to benefit from the auxetic effect. The inverted honeycomb cell is again of interest, but for a different property. It can be seen as a truss structure composed of elastic beams. The goal is then to constrain the radial expansion, bending, shearing and torsion of the actua-

tor thanks to the truss structure, while exhibiting a higher axial compliance and favoring the axial extension of the structure under pressure thanks to its geometry (see Fig. 4). This actuator will be designated in the following as an auxetic reinforced actuator and will be presented in section 4.

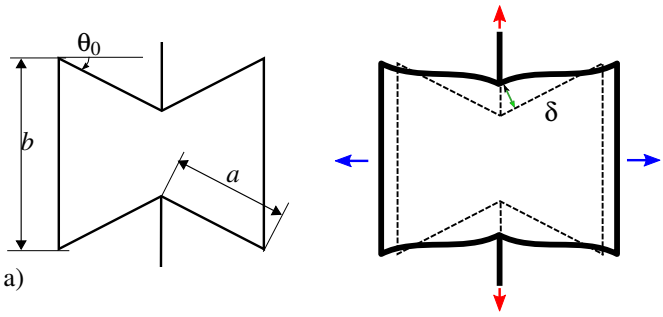

Fig. 4. Parametrization and deformation of the auxetic cell under axial strain.

2.4 Manufacturing process

Although a combination of flexible and stiff materials can be achieved through various methods and processes [42], MMAM is considered with use of purely-additive inkjet printing technology (Stratasys Polyjet [43]). This choice is motivated by three reasons. First, it is a convenient method to produce at the same time both the inflatable structure and the guiding skeleton of the actuator, as well as any required interface part for actuator integration. This should be in favor of actuator compactness. Second, the use of polymers makes the implementations compatible with a future use in image-guided robotics, as outlined in the introduction. Third, among the possible MMAM processes (multi-step with shape deposition manufacturing [44], direct ink writing, HP Multi Jet Fusion, Arburg APF), the Polyjet process provides interesting resistance of interfaces between materials as observed in a previous work [33].

All geometries and dimensions are chosen to be compatible with the process specifications [45]. In particular, minimum thickness of materials of 1 mm is respected, as well as the need to remove support material when producing hollow structures. In the following, 'stiff' and 'rubber-like' materials will respectively refer to the VeroWhite and TangoBlack Plus materials, according to their trade names [43]. Their Young's modulus are respetively equal to 2 GPa and 1 MPa. Previous characterization showed that the rubber-like material can endure elongation up to 60%, and that a maximum yield stress of 25 MPa has to be respected for stiff structures [45]. This will be our resistance criteria during the actuator synthesis.

3 Deployable pocket actuator

The first way to design the actuator is to use the inverted honeycomb cell as an articulated pocket which internal volume increases during its deployment. The main inspiration comes from previous work such as an inflatable inverted honeycomb cell network proposed by Vos *et al.* [38] as a shape morphing structure for aerospace applications.

Fig. 3a shows how the inverted honeycomb cell can be used to create a deployable mechanism. The actuator central part is obtained by extruding this base articulated shape, forming an open prismatic tube with rigid faces and revolute joints along the faces vertices. The convexity of the lateral arms of the hexagonal section has a direct impact on its performance. For the concave shape (inverted honeycomb with $\theta < 0$), the surface area of the cell increases monotonically with L and the maximum extension is reached for $L_{\max} = 2a$. In contrast, the convex shape area ($\theta > 0$) reaches its maximum for the extension $L' = \frac{1}{2}\sqrt{2\sqrt{b^4+8a^2b^2}+8a^2-2b^2} < 2a$ as illustrated on Fig. 3b. Consequently, the inverted honeycomb shape is of particular interest for two reasons: 1) it provides the highest extension and 2) it has a reduced footprint with a maximum width of b, compared to $2a+b$ for the convex shape in the fully folded ($\theta = \pm\pi/2$) configuration.

In order to form a fully closed pocket, the hollowed inverted honeycomb structure is closed with additional faces. The pattern used for these closures is inspired by the origami "waterbomb" pattern. Four out of the six faces of both these end caps have been chosen as soft in order to allow the deformations required for the chamber deployment under pressurization. At this point, chamber closures could be set toward the interior or the exterior of the actuator. The latter option has been selected, favoring integration commodity over a small gain in performance and compactness. Some additional design details can be found in [46].

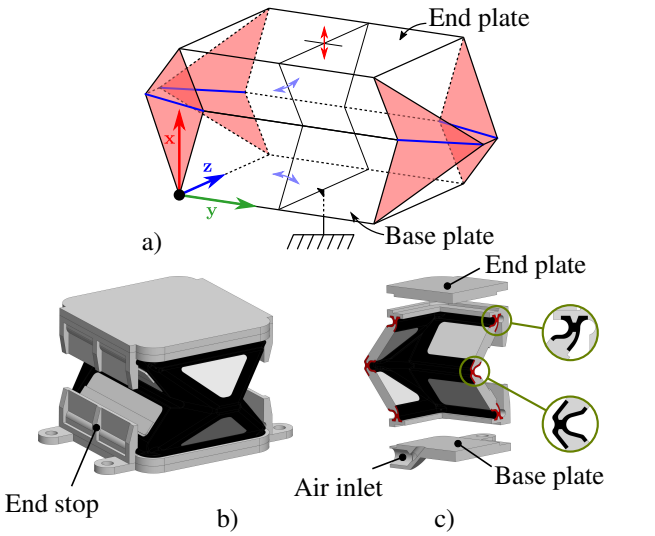

Fig. 5. a) Geometry of the polyhedral pocket highlighting both the deformable faces (in red) and the variable length edges (in blue). b) CAD view of the actuator and c) exploded view of a quarter cutout with details on the hinges geometry. The rigid and rubber-like materials appear in gray and black respectively.

The resulting polyhedric volume obtained is detailed in Fig. 5a. Faces and edges highlighted in red an blue indicate areas which need to be deformable for the design to function properly. For evaluation, the geometry was selected keeping in mind actuator performance and manufacturing constraints. The chosen dimensions [46] are $b = 35$ mm and $w = 40$ mm as the base dimensions, with w being the extrusion length of the inverted honeycomb cell. The arm length is $a = 16$ mm, and the initial length of the actuator is set to $L_0 = 22$ mm.

The final design is obtained by creating a quasi-monolithic system combining rigid articulated panels with deformable areas. The CAD view of the obtained prototype is shown in Fig. 5b and c. Flexure hinges as well as the deformable areas in the chamber closures are made of rubber-like material as depicted in Fig. 5c. Angular end-stops are also added to both the base and the end plate in order to stop the deployment of the inverted honeycomb pattern. Without these limits, the cell would then possibly change from inverted to classical honeycomb configuration. Indeed, as illustrated in Fig. 3b, the maximum volume is reached at a lower extension value in the classical honeycomb cell configuration.

The hinges are submitted to complex sollicitations during deployment with bending, shearing and traction of the rubber-like material. It is then difficult to establish a static model for the actuator. To favor smooth changes in material properties and limit the stress in the hingers, transition areas are created by adding a thin layer of rubber-like material on the rigid panels near the hinges. Finally, both base and end plates are manufactured separately from the rest of the actuator and then glued on it to easily access the internal volume for support material removal operations.

4 Auxetic reinforced actuator

The second way to design the actuator is to use a pattern of inverted honeycomb cells used as an auxetic reinforcement structure. Auxetic structures are usually considered for meta-material design [47–49] but scarcely in robotics [50, 51] as an efficient way to design new soft actuators. To design a tubular pneumatic actuator, one can consider a simple hollow cylinder as depicted in Fig. 6a). The lateral wall of the hollow cylinder is made of homogeneous elastic material to get a reversible behavior, using in particular a rubber-like material to have large admissible deformations whereas its end caps are made of rigid, non-deformable material. When submitted to an internal pressure P, the lateral wall deforms, and as consequence the cylinder shape is radially and axially deformed as shown in Fig. 6b). Depending on the cylinder geometry (diameter, height and thickness of the walls), the resulting displacement of the top surface toward the lengthening of the actuator is mitigated by the radial expansion of the actuator which is detrimental to the actuator efficiency, as it tends to decrease the cylinder length. The auxetic structure is here used on purpose to obtain a cylinder lateral wall which material has a negative Poisson's ratio. In these conditions, the pressure on the lateral wall induces the lengthening of the cylinder, so the detrimental antagonistic effects are suppressed as depicted in Fig. 6c).

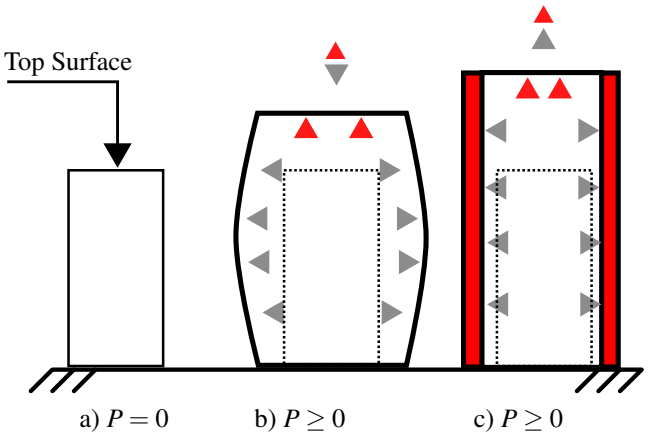

Fig. 6. Section view of the chamber: a) without pressure; b) with pressure, conventional outer envelope; c) with pressure, auxetic reinforced outer envelope. Axial and radial forces produced by internal pressure are represented by red and gray arrows.

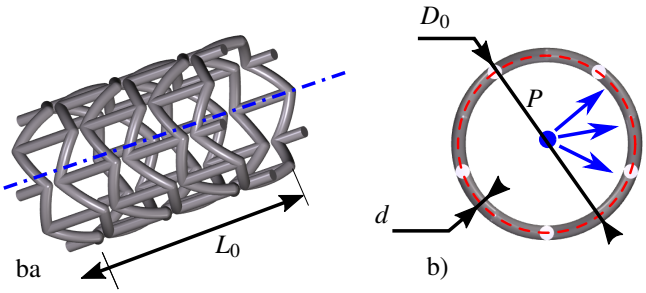

Fig. 7. a) the auxetic structure and b) its circular section.

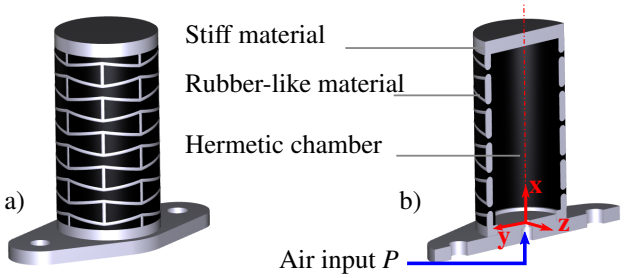

Fig. 8. a) CAD view of the complete auxetic actuator with b) cross-sectional detailed view.

The actuator lateral wall structure is therefore based on the repetition of the inverted hexagonal honeycomb cell. This unit cell, described and parametrized in Fig. 4 is circularly repeated to create a ring and several rings are then connected along the axial direction to obtain the auxetic structure depicted in Fig. 7b) and c).

Another advantage of the auxetic structure is its continuity as the pattern is wrapped around the actuator (Fig. 8a).

a	length of the slanted strut
b	length of the vertical strut
θ_0	inclinaison of the slanted strut
d	diameter of the strut
N_c	number of unit cells along the circumference
N_v	number of unit cells along the length
D_0	nominal diameter of the cylinder
L_0	nominal length of the cylinder
t_m	thickness of rubber-like material for sealing

Table 1. Parametrization of the auxetic structure geometry.

This favors the off-axis stiffness which is very interesting to obtain satisfying kinematic behavior without the need to introduce additional guidance in parallel with the actuator. In Fig. 8b), a cross-sectional view of the actuator is represented. One can identify the auxetic structure and an inner tube made of rubber-like material to create a hermetic chamber. This material is used to create the inner envelope and it is also placed between the struts of the auxetic structure in order to improve the structural strength. An outer envelope made of the same rubber-like material has been also added in order to further increase the resilience of the actuator, but this envelope is not represented in Fig. 8a) for the sake of clarity, and is only visible in Fig. 1.

The auxetic structure is described by nine parameters introduced in Fig. 4a), Fig. 7a) and b) and listed in Table 1. Because of the inverted honeycomb cell and the way the unit cells are assembled, two relationships can be written:

$$b = \frac{L_0}{2N_v} + a\sin\theta_0 \tag{1}$$

$$a = \frac{\pi D_0}{2N_c\cos\theta_0} \tag{2}$$

When the hermetic chamber is pressurized, the axial deformation results from the deformation of structure composing the inverted honeycomb cell, as depicted in Fig. 4a). The model describing this deformation was derived in [48]. The chamber of the actuator is composed of three layers (see Fig. 8). External and internal layers are made with the rubber-like material to ensure the chamber sealing, with a thickness of t_m. The Young's modulus of this material is denoted as E_2. The third layer corresponds to the auxetic structure, where the presence of rubber-like material between the beams of the truss is neglected. This third layer is then characterized by the material properties described by four parameters (see the model description in appendix): the Young's modulus in the axial direction E_x, the Young's modulus in the circumferential direction E_c, the Poisson's coefficient ν_{xc} describing the ratio between tube circumferential and axial contractions when submitted to an axial load, the shear modulus G_{cx} describing the ratio between the shear stress in the tube wall and the corresponding shear strain. E_1 is the Young's modulus of the stiff material used for the auxetic structure. The static model relates the pressure P in the actuator chamber, the force F generated by the actuator at its end, and its elongation denoted as $\Delta L = L - L_0$. Its derivation was performed for McKibben actuators [36] using the principle of virtual work. With the same approach [52], it comes that:

$$\Delta L = \frac{-F + \frac{\pi}{4}PA\left(A - \frac{2D_0}{\nu_{cx}}\right)}{\Sigma_x + 2\pi\Sigma_c\frac{D_0^2}{\nu_{cx}^2}}L_0 \tag{3}$$

with

$$\begin{aligned} A &= D_0 - d - 2t_m \\ \Sigma_x &= S_0(E_x + E_2) + (S_1 + S_2)E_2 \\ \Sigma_c &= \frac{(E_c + E_2)d}{D_0} + \frac{E_2 t_m}{D_0 - d - t_m} + \frac{E_2 t_m}{D_0 + d + t_m} \end{aligned}$$

Stiffness expressions can be derived as well using beam theory as provided in appendix. The flexural stiffness, i.e. the off-axis stiffness K_y, is of particular importance to obtain a linear extension along $\mathbf{x}$ without any additional mechanical linear guidance.

The geometrical parameters of the inverted honeycomb cell influence the performances of the actuator, and some design rules can be established. It is indeed easy to describe the sensitivity of elongation and stiffness to geometrical variations. Increasing the actuator length L_0 improves the elongation ΔL but decreases the stiffnesses. The stiffnesses are directly proportional to the number of cells wrapped around the actuator N_c and the actuator elongation ΔL is inversely proportional to this number. Increasing the outer diameter D_0 increases the displacement ΔL but decreases the stiffnesses. Enlarging the diameter without modifying any other geometrical parameter indeed distorts the auxetic structure with lowers actuator stiffness. Increasing the diameter d of the struts in the auxetic structure is favorable to the stiffness but lowers the elongation.

The diameter of the struts d affects the bending stiffness of the struts $K_{\theta,z}$, the torsional stiffness $K_{\theta,x}$ and consequently all properties of the actuator. By modifying d, a large range of actuator performances can be covered. It also of course implies a high sensitivity of the actuator behavior to such a parameter in the manufacturing. The influences are summarized in Table 2.

The synthesis of actuator depends on the desired tradeoff between the elongation ΔL and the flexural stiffness K_y. Some geometrical constraints also exist on the geometry of the auxetic structure. The inverted honeycomb can be produced without geometrical interferences in the cell shape if the value of θ belongs to $]0, \frac{180}{\pi}\arcsin\left(\frac{b-d}{2a}\right)]$. The elastic material also has a limited stress domain. Maximum stress $\sigma_{max} = \frac{3E_1 dL_0\varepsilon_x}{2N_v a^2}$ is encountered in the slanted struts of the auxetic cells, submitted to bending, with an overall displacement of the structure with the dimensions possibly limited by the manufacturing process.

L_0	N_c	D_0	d	Influence
↗	↘	↗	↘	ΔL ↗
↘	↗	↘	↗	K_y ↗
↘	↗	↘	↗	$K_{\theta,z}$ ↗
↘	↗	↘	↗	$K_{\theta,x}$ ↗

Table 2. Sensitivity of the elongation and the stiffnesses to the geometrical parameters.

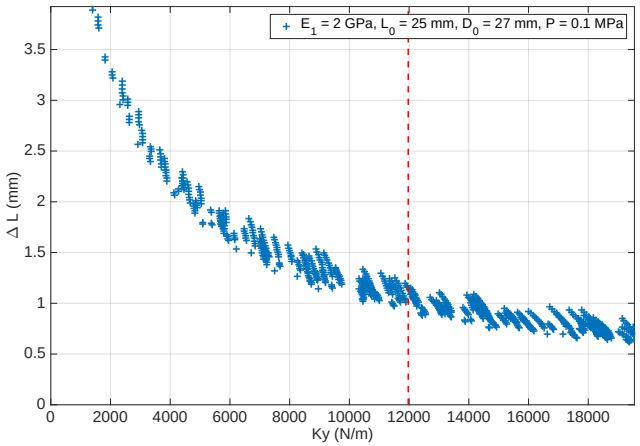

Fig. 9. Evolution of the chamber elongation ΔL with respect to the flexural stiffness $K-y$. In dashed red line, the expected minimum goal stiffness.

For the experimental evaluation, the actuator synthesis is performed by setting first the size of the actuator. The outer diameter of the actuator is chosen to keep it compact and compatible with an integration in a robotic device for needle manipulation such as the one presented in [53]: $D_0 = 27$ mm, $L_0 = 25$ mm. The actuator volume is then comparable to the one of the inflatable pocket actuator, which will ease the comparison during the discussion.

The selection of the geometry is performed by plotting all possible values of displacement ΔL and stiffness K_y after a discretization of the geometrical parameters: $N_c \in [3,5]$ step 0.5, $N_v \in [1,4]$ step 0.5, $\theta_0 \in [5,15]$ step 1° and $d \in [1.5,2.5]$ step 0.1 mm. For each combination of geometrical parameters, the value of ΔL is computed then verified in order that $\theta < \theta_{max}$, $\sigma_{max} < 25$ MPa, and that the stiffness K_y is at least five times stiffer than a 1-mm steel rod with a length of 25 mm, which means $K_y \geq 12$ N/mm. The possible performances are plotted in Fig. 9. The dashed red line is the minimum expected flexural stiffness of the chamber. All the geometries that respect the three constraints are compared and the geometry that presents highest value of ΔL is chosen. Fig. 10 shows the influence of the strut diameter d on the chamber elongation for different pressure levels. One can notice the high sensitivity of the actuator elongation to this diameter. An elongation ΔL = 1.1 mm can be obtained for a P = 100 kPa pressure when choosing a diameter d equal to 1.7 mm. The off-axis stiffness is then still satisfactory with $K_y \approx 12$ N/mm. It was observed in [54] that variations of dimensions can reach 0.5 mm when producing details such as 2-mm beams within a layer of soft material, because of the material gradients automatically created during the production. In order to ensure the diameter d is at least equal to 1.7 mm, it is decided to select d = 2.2 mm. The final geometry is defined by $(D_0, L_0, N_c, N_v, \theta_0, d) = (27\,\text{mm}, 25\,\text{mm}, 4, 2.5, 10°, 2.2\text{mm})$. In order to ensure the airtightness of the chamber, the inner and outer tube thicknesses have been chosen to be equal to 0.65 mm.

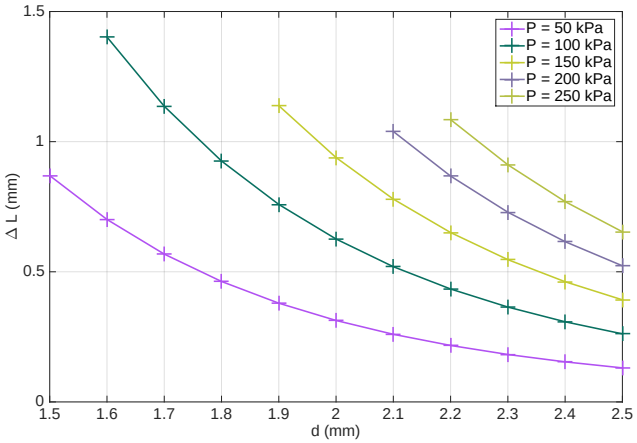

Fig. 10. Evolution of the elongation ΔL with respect to the diameter d for different pressure levels.

5 Results

The behavior of the two proposed soft actuators has been analyzed through experimental characterization. The comparison is performed under two conditions: 1) a characterization of the maximum displacement without load, and 2) a characterization of the maximum load in static condition. These tests are complemented with cyclic tests in both conditions in order to assess the repeatability and lifetime of the actuators. For the auxetic reinforced actuator, additional characterization is achieved to establish the off-axis stiffness, as it is a specific property of the actuator. In order to control the actuators during these tests, a pneumatic distribution bench was designed as shown in Fig. 11. It is composed of a proportional valve (VPPM series, Festo) for the pressure regulation and a fast 3/2-way solenoid valve (MHE2 series, Festo) to trigger the output. The air pressure delivered by this stage is measured with a pressure sensor (SPTW series, Festo). A custom software running under a real-time operating system (Linux Xenomai) is used to synchronize all sensor acquisitions with the control of the distribution at a sampling rate of 1kHz. For both actuators, preliminary assessments of the maximum pressure were carried out in order to define the maximum working pressure that preserves

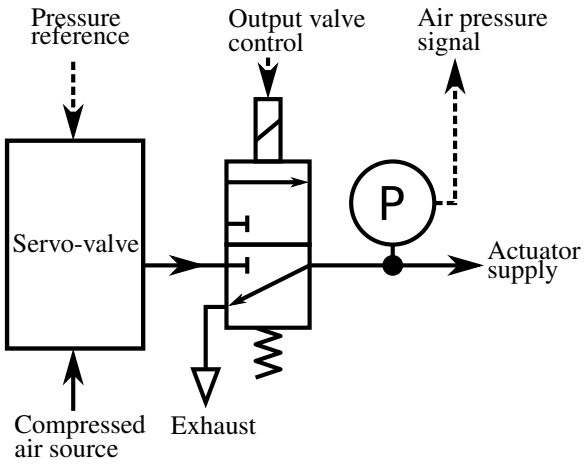

Fig. 11. Pneumatic control bench used during the characterization experiments.

the actuator integrity during tests. The identified maximum pressure was 250 kPa for the auxetic reinforced actuator, and 25 kPa for the pocket deployable actuator. In both cases, the actuator failure is related to the tearing of the rubber-like material that leads to pressure losses.

5.1 Displacement characterization

The first experiment carried out on both actuators was a displacement characterization with a setup described in Fig. 12. In this test, the actuators were allowed to move freely without load and several steps of increasing pressures were applied. The displacements was then measured using a laser telemeter (OptoNCDT 2300 series, Micro-Epsilon) and synchronized with the distribution control.

Fig. 12a) and b) show the setup and results of the displacement characterization for the auxetic and the deployable actuator. In the presented plots, ε represents the relative displacement of the actuator, computed as $\varepsilon = \Delta L/L_0$, where ΔL and L_0 denote respectively the displacement and the initial length (i.e. its length in the resting position without inflation) of the actuator. Fig. 12c) and d) show the transient response of the actuators for several air pressures. Both actuators show at first an extension followed by a slower stabilization phase. This phenomenon is due to the creep of both the rigid and soft materials. Fig. 12e) and f) represent the maximum relative displacement at several pressure levels, expressing both actuators steady-state displacement/pressure relationship. As pressure increases, the maximum relative displacement also increases due to the intrinsic stiffness of the actuators.

For the auxetic actuator, the observed relative displacement shows a maximum of about 10.7% at a pressure of 250 kPa, corresponding to a displacement of about 2.68 mm. Up to 200 kPa, the relative displacement/pressure relationship is mostly linear with an experimental slope of 38.6 MPa^{-1}, that is compared to 44 MPa^{-1} as the result of actuator synthesis. This is advantageous in order to create linear motion similarly to stepper motor, where precisely

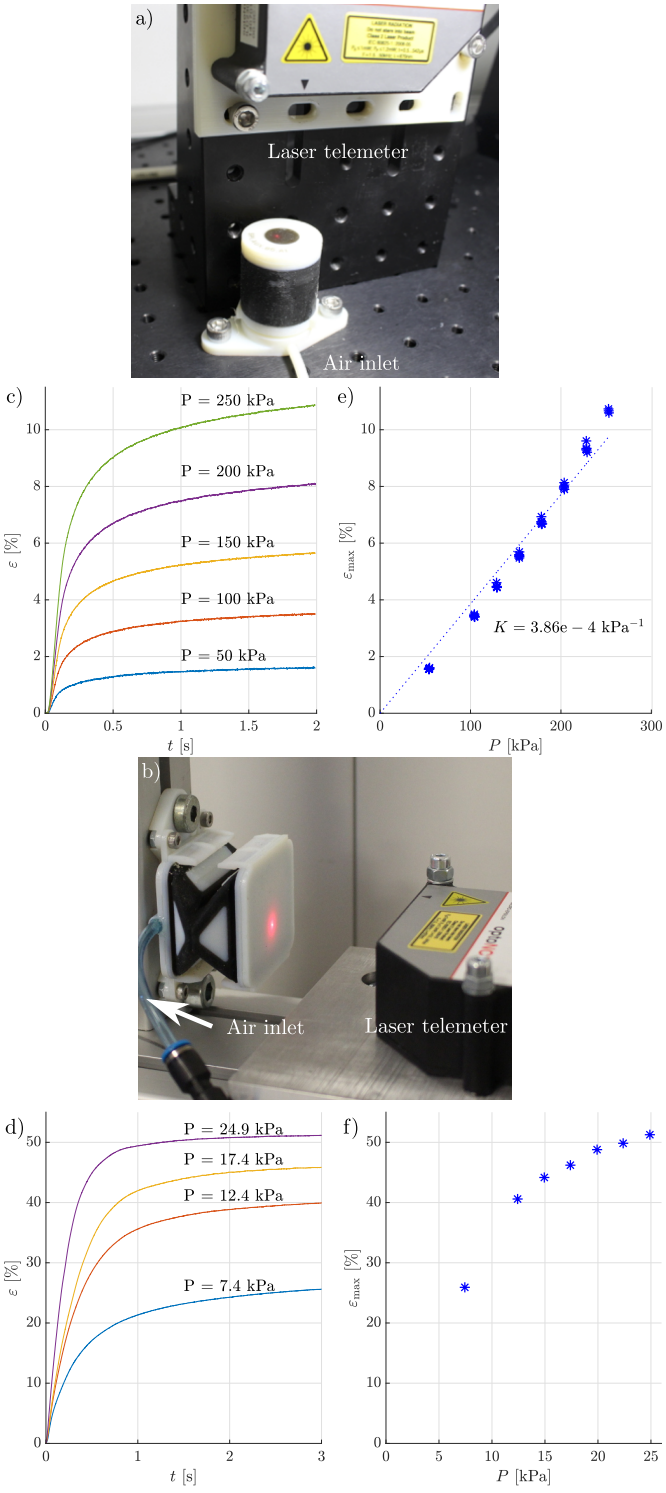

Fig. 12. Configuration of the displacement test for a) the auxetic actuator and b) the deployable actuator. Relative displacement without load at various pressures with respect to time for c) the auxetic actuator and d) the deployable actuator. Maximum relative displacement without load with respect to the pressure for e) the auxetic actuator and f) the deployable actuator.

controlling the step is more important than having a large step size. However, for a 100 kPa internal pressure, the expected displacement of the actuator should be roughly

1.1 mm, but the experimental results give a displacement of 0.88 mm.The difference can be explained by the fact that the manufacturing process could not ensured the shape and the diameter of the auxetic struts and the external rubber like membrane increases the longitudinal stiffness that can not be include in the synthesis.

For the deployable actuator, the observed relative displacement shows a maximum of 51.3% at a pressure of 24.9 kPa, corresponding to a maximum displacement of about 11.3 mm. This allows the actuator to create quite large range displacements with respect to its initial length. As a comparison, McKibben muscles usually exhibit relative displacements in the 10 to 30% range [25], vacuum buckling muscles up to 40% [22] and paper-reinforced silicon rubber origami actuators up to 300% [40].

In a previous study [46] where the model was obtained following pseudo-rigid kinematics, the maximum displacement obtained was 10 mm ($\varepsilon = 45.5\%$). The slightly greater experimental value could be explained by the initial model not accounting the longitudinal strain of the hinges that results from the tension of the end plate. This means that the actual strain level is higher than initially expected, with a potential negative impact on the material resistance and actuator lifetime.

5.2 Force characterization

The second type of experiment carried out with the actuators was a static force characterization. In this test, the extension of the actuators was blocked by a 100N force sensor (K1563, Scaime) in order to measure the force generated by both actuators in their rest configuration under several steps of pressure. In order to avoid transmitting torques and normal forces that could disturb the measures, the contact between the sensor and the actuator is achieved thanks to an hemispheric finger. The force measured in this experiment represents the maximum force the actuator can apply as the elastic deformation should be minimal in this state. The setup and results of the static force characterization are displayed in Fig. 13a) and b). Fig. 13c) and d) show the transient response of both designs to the pressure steps. The actuators force response exhibits a fast increase, followed by an almost constant value once stabilized. Fig. 13e) and f) show the maximum force/pressure relationship of both actuator at different pressure levels. Both actuator show a quasi-linear behavior and can thus be described with an equation $F_{\max} = k_1 P$. The slope k_1 corresponds to the surface area of the equivalent pneumatic cylinder with similar force-pressure behavior.

The auxetic actuator produces a maximum force of 30.1 N at a pressure of 250 kPa, with an effective surface area of about 117 mm^2. This represents only 28% of the actual internal surface area of 430 mm^2 (room diameter: 23.5 mm). Such efficiency is probably due to the contraction of the soft material. Indeed, the elastic behavior of the auxetic structure gives the actuator some axial stiffness that is still detrimental to the actuator extension.

At the pressure of 24.9 kPa, the maximum force measured on the deployable actuator is 33.2 N, with the actuator effective surface area of 1410 mm^2. This value is quite com-

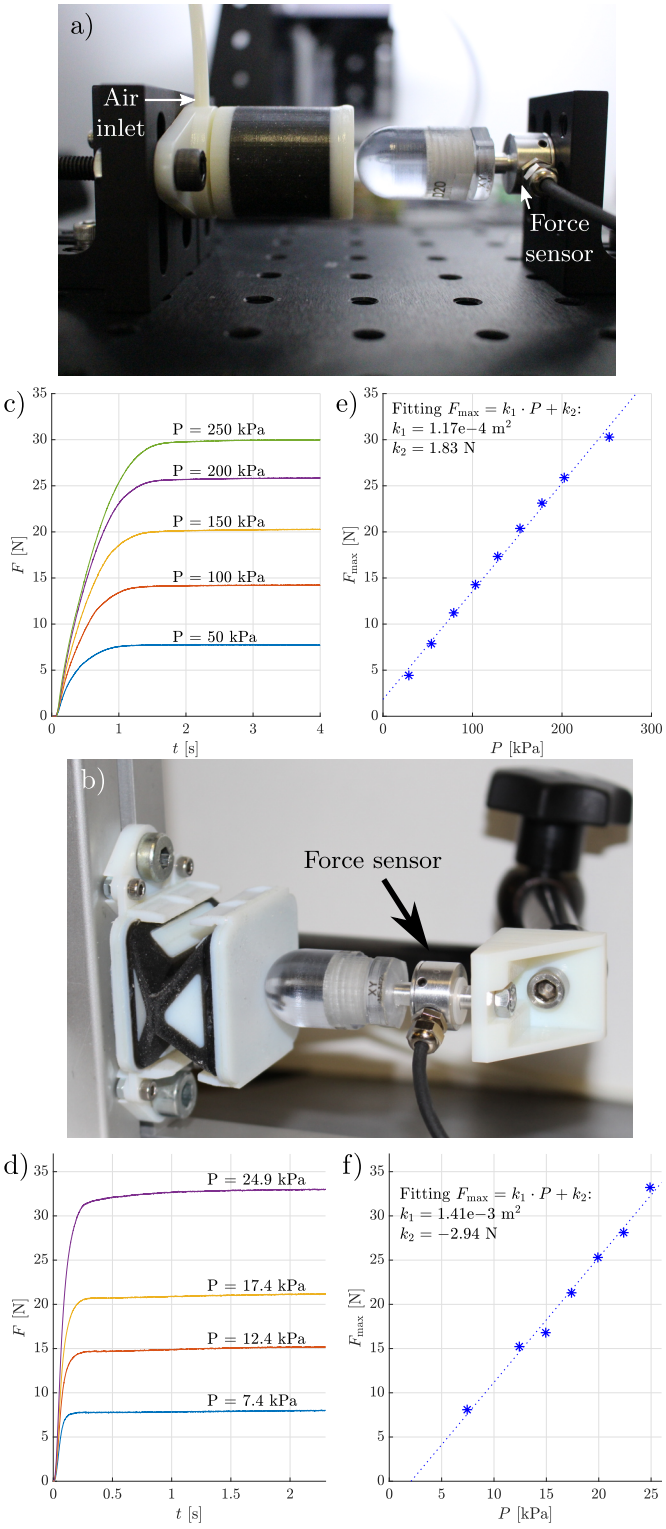

Fig. 13. Configuration of the force test for a) the auxetic actuator and b) the deployable actuator. Static force response generated by c) the auxetic actuator and d) the deployable actuator at various pressures with respect to time. Maximum force generated by e) the auxetic actuator and f) the deployable actuator with respect to the pressure.

parable to a rectangular piston with the same footprint, i.e. with a surface area $wb = 1400$ mm^2. This shows the ability of the actuator to convert most of the pressure into actual force with a maximum efficiency similar to that of a frictionless pneumatic cylinder with the same piston surface.

5.3 Cyclic loading

Some major concerns related to actuator manufactured with soft material are both their viscoelastic behavior and also their material strength. While actuation steps give an estimate of the actuator dynamic performance, they do not provide insights on the actuator repeatability and lifetime. To this end, cyclic loading tests have been carried out. In those tests, the actuators have been positioned in similar conditions to the ones enforced during the step tests, with input pressure set to an intermediate value of 150 kPa for the auxetic actuator and 17.4 kPa for the deployable actuator. The commutation valve was then toggled within a 8 s time frame in order to obtain a square pressure signal. The period has been chosen in order for each actuator to reach its equilibrium before switching on or off the pressure. During each period, the maximum relative displacement/force value was measured, and the total number of cycles were calculated. Tab. 3 sums up the results obtained. After more than 10^2 cycles, the auxetic actuator was still working properly. In addition the actuator shows a very good repeatability in both force and relative displacement. This is particularly interesting for the application, as it allows a higher precision for positioning tasks.

Actuator	P [kPa]	ε_{max} [%]	F_{max} [N]
Auxetic	150	6.1 [0.09]	20.3 [0.03]
Deployable	17.4	47.2 [0.48]	24.4 [0.44]

Table 3. Cyclic loading performances of both actuators. The values displayed are the mean and standard deviation of the maximum relative displacement and the maximum force measured during each cycle.

The deployable actuator started to fail between 25 and 30 cycles during the displacement test but was still operational after more than 60 cycles in the force test. This discrepancy is probably due to the higher strain level generated by the structure deformation during displacement tests. The force tests being carried out in a static configuration, the strain level is *a priori* more limited. Cyclic performance shows a lower repeatability than with the auxetic actuator, most probably due to the higher axial compliance.

5.4 Flexural stiffness evaluation for the auxetic reinforced actuator

The off-axis stiffness of the actuator is assessed by determining its flexural stiffness. The actuator is in an horizontal configuration, so that transverse loading may easily be performed using weights suspended at the free end of the actuator, as shown in Fig. 14a. The corresponding displacements of the actuator end are measured by vision (camera Canon®EOS 700D, 18-55 mm, 18 MPixel resolution). The load-deflection curve built experimentally is presented in Fig. 14b. The flexural stiffness, K_y, can be estimated from this characteristics as the inverse of the slope of the linear model interpolated from the experimental data. This stiffness value is estimated equal to 7.9 N/mm, lower than value of 12 N/mm provided by the model. The uncertainties of struts geometry have to be the main sources of difference between theoretical value and experimental value.

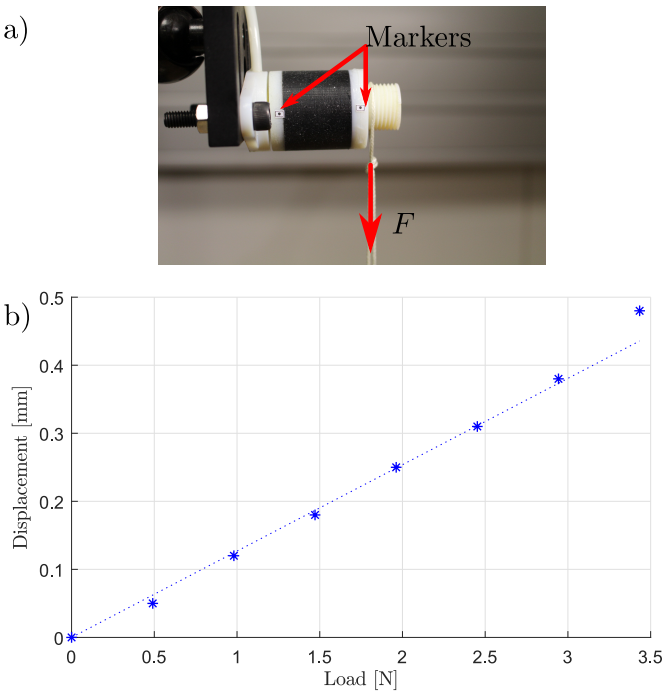

Fig. 14. a) Experimental setup for the measurement of the flexural stiffness of the auxetic-based actuator. b) Load-deflection characteristics for the determination of the flexural stiffness value.

6 Discussion

In this article, we have presented the design of two soft pneumatic extension actuators, starting from the exploitation of the inverted honeycomb cell either as an articulated mechanism or a compliant structure.

Using a single cell, an inflatable pocket actuator was designed and tested. Inspiration from origami shapes was necessary to create the closed pocket. The stroke to length ratio was measured to be 50%. The blocked force is 33.2 N, which corresponds to a specific stress of 0.02 MPa, using the criterion from [52]. The measured response time is between 0.8 and 1.94 seconds. The highest value of time response is probably due to the dynamics of servo-valve for very low pressure. Based on a pattern of inverted honeycomb cells, the other actuator has rather complementary performances. The stroke to length ratio is much smaller, in the order of 10%. However the specific stress is equal to 0.01 MPa, almost one

order of magnitude higher than the inflatable pocket actuator. The response time is between 0.97 and 1.15 seconds.

The range of motion of the actuators is obviously much more limited than a conventional pneumatic cylinder. However the actuators are quasi monolithic, which can be of interest to design them within a more complex assembly, without constraints related to their integration. This can be an advantage in terms of compactness in a system development. In addition, the maximum force of the inflatable pocket actuator is comparable to the one of cylinders with the same footprint, with the advantage of no dry friction. The auxetic reinforced actuator has the same advantage of absence of dry friction. In addition, it can be designed to avoid any additional component for guidance, as needed with a cylinder. Control of motion can then be simplified, especially if high resolution motions are expected.

The specific stress and the stroke to length ratio, in other words the admissible strain, makes them comparable to pneumatic artificial muscles. But it is worth noting first that the performances of the actuators represent an extension of the specific stress-deformation space defined by usual pneumatic artificial performances. The 50% strain is above performances of commercial McKibben artificial muscles. The auxetic reinforced actuator has half the strain offered by these muscles. However, the use of inverted honeycomb cells makes it possible to control the off-axis stiffness. The two actuators provide extension linear actuators, which can be in addition of interest as it provides design freedom for integration.

The performances of the actuators make them comparable in some ways to McKibben artificial muscles. In terms of application contexts, this helps to define the primary fields of applications where they can be of interest, with first the medical field, our initial motivation. The auxetic reinforced actuator could be designed with a sufficient stiffness to drive surgical tools such as medical needles. The displacement provided by the actuator can then be used in a step by step motion as considered in inchworm motors [35, 36]. If the range of motion of the actuators is too restricted, step by step kinematics can indeed be used, in a similar manner as for actuation technologies like shape memory alloys or piezoelectric actuators. The main second field of application is assistive and service robotics where the compliance, in particular, is of interest.

The design approach used in our study is combined to a manufacturing strategy based on MMAM. In our opinion, this work shows their combination is of high interest because of the freedom of shape and mechanical properties within the inflatable structure. In this way, this work opens the way to further design work to closely link kinematic analysis and properties of materials, in particular using gradients of materials. The level of performances of the actuators is today linked to the failure modes of the soft material, so specific work should be conducted on this aspect. Alternate hybrid production of the two actuators could be considered if necessary, such as the additive manufacturing of the elastic parts, before over-molding the elastomeric envelope. Another interesting perspective will be to follow the design approach we adopted, which is to build actuators from a given cell employed either as an articulated mechanism or a deformable structure, and apply it to other geometrical patterns. This can be seen as a way to have convergence between metamaterial designs and origami-based designs. It also offers novel solutions to customize actuators for service robotics where integration and compliance are challenges. However, some technical difficulties remain for the inflatable pocket actuator, for which the complex solicitations of hinges make it difficult to establish static models. The development of these models remains an open subject.

Acknowledgements

This work was supported by the Investissements d'Avenir (Robotex ANR-10-EQPX-44, Labex CAMI ANR-11-LABX-0004) and by the Region Grand Est and the FEDER (European Funds of Regional Development) under Interreg V program, SPIRITS project. We would like to thank Quentin Boehler, Arnaud Bruyas, Mathieu Nierenberger and Benoît Wach for their help and contribution in the development, improvement and assessment of the auxetic actuator.

Appendix: Equivalent model of auxetic structure

It was shown that it is possible to describe the auxetic structure behavior by considering this latter as a continuous tube made of an homogeneous material, orthotropic to be representative of the auxetic behavior. The material properties of this Homogeneous Auxetic Structure (HAS) are directly linked to the unit cell geometry and the number of cells in the tube. As given by Karnessis et al. [48], four coefficients are then sufficient to describe the behavior of the equivalent tube when submitted to the internal pressure:

$$E_x = \frac{3E_1\left(\frac{b}{a}-\sin\theta_0\right)}{2\pi^2}\left(\frac{dN_c}{D_0}\right)^3$$

$$E_c = \frac{3E_1\cos^2\theta_0}{2\pi^2\left(\frac{b}{a}-\sin\theta_0\right)\tan^2\theta}\left(\frac{dN_c}{D_0}\right)^3$$

$$\nu_{cx} = -\frac{\cos\theta_0}{\left(\frac{b}{a}-\sin\theta_0\right)\tan\theta_0}$$

$$G_{cx} = \frac{3E_1\left(\frac{b}{a}-\sin\theta_0\right)\cos^2\theta_0}{2\pi^2\left(\frac{b}{a}\right)^2\left(1+\frac{2b}{a}\right)}\left(\frac{dN_c}{D_0}\right)^3$$

The stiffness of the actuator can be expressed by considering the three layers are placed in parallel and connected altogether to the actuator tip.

Using beam theory, flexural stiffness in the **y** direction is defined as the ratio between a force in the **y** direction and the corresponding translation:

$$K_y = \frac{3E_xI}{L_0^3} + \frac{3E_2I}{L_0^3} + \frac{3E_2I_1}{L_0^3} + \frac{3E_2I_2}{L_0^3}$$

This stiffness is proportional to E_x, the second moment of inertia of the homogeneous auxetic structure, the Young's modulus of the soft material and inversely proportional to L_0^3. The rotational stiffness along the **z** direction is defined as the ratio between a force in the **z** direction at the tip and the corresponding rotation:

$$K_{\theta,z} = \frac{2E_xI}{L_0^2} + \frac{2E_2I}{L_0^2} + \frac{2E_2I_1}{L_0^2} + \frac{2E_2I_2}{L_0^2}$$

This stiffness is proportional to E_x, the second moment of inertia of the homogeneous auxetic structure, the Young's modulus of the soft material and inversely proportional to L_0^2. The torsional stiffness along the **x** direction is defined as the ratio between a moment in the **x** direction and the corresponding rotation:

$$K_{\theta,x} = \frac{G_{cx}I}{L_0} + \frac{G_2I}{L_0} + \frac{G_2I_1}{L_0} + \frac{G_2I_2}{L_0}$$

This stiffness is proportional to G_{cx}, the second moment of inertia homogeneous auxetic structure and Young's modulus of the soft material and inversely proportional to L_0. And the axial stiffness in the **x** direction is defined as the ratio between a force in the **x** direction and the corresponding translation:

$$K_x = \frac{SE_x}{L_0} + \frac{SE_2}{L_0} + \frac{S_1E_2}{L_0} + \frac{S_2E_2}{L_0}$$

This stiffness is proportional to E_x, the surface of tubes in perpendiculaire plane to their axis, Young's modulus of the soft material and inversely proportional to L_0. The second moment of inertia of the each layers are I for HAS, I_1 for external soft layer, I_2 for internal soft layer, G_2 is the shear modulus of soft material. S, S_1 and S_2 are respectively the surfaces of layers in the plane perpendicular to their axis.

References

[1] Best, C. M., Wilson, J. P., and Killpack, M. D., 2015. "Control of a pneumatically actuated, fully inflatable, fabric-based, humanoid robot". In IEEE-RAS 15th International Conference on Humanoid Robots (Humanoids), pp. 1133–1140.

[2] Hawkes, E. W., Blumenschein, L. H., Greer, J. D., and Okamura, A. M., 2017. "A soft robot that navigates its environment through growth". *Science Robotics,* **2**(8), July, p. eaan3028.

[3] Ranzani, T., Gerboni, G., Cianchetti, M., and Menciassi, A., 2015. "A bioinspired soft manipulator for minimally invasive surgery". *Bioinspiration & Biomimetics,* **10**(3), p. 035008.

[4] Wehner, M., Quinlivan, B., Aubin, P. M., Martinez-Villalpando, E., Baumann, M., Stirling, L., Holt, K., Wood, R., and Walsh, C., 2013. "A lightweight soft exosuit for gait assistance". In IEEE International Conference on Robotics and Automation (ICRA), pp. 3362–3369.

[5] Polygerinos, P., Wang, Z., Galloway, K. C., Wood, R. J., and Walsh, C. J., 2015. "Soft robotic glove for combined assistance and at-home rehabilitation". *Robotics and Autonomous Systems,* **73**, Nov., pp. 135–143.

[6] Mazzolai, B., Margheri, L., Cianchetti, M., Dario, P., and Laschi, C., 2012. "Soft-robotic arm inspired by the octopus: II. From artificial requirements to innovative technological solutions". *Bioinspiration & Biomimetics,* **7**(2), p. 025005.

[7] Cianchetti, M., Calisti, M., Margheri, L., Kuba, M., and Laschi, C., 2015. "Bioinspired locomotion and grasping in water: The soft eight-arm OCTOPUS robot". *Bioinspiration & Biomimetics,* **10**(3), p. 035003.

[8] Kim, Y., Cheng, S. S., and Desai, J. P., 2018. "Active stiffness tuning of a spring-based continuum robot for mri-guided neurosurgery". *IEEE Transactions on Robotics,* **34**(1), pp. 18–28.

[9] Yang, Y., Chen, Y., Wei, Y., and Li, Y., 2016. "Novel Design and Three-Dimensional Printing of Variable Stiffness Robotic Grippers". *ASME Journal of Mechanisms and Robotics,* **8**(6), Sept., p. 061010.

[10] Paulino, G. H., Qi, H. J., Wu, J., and Liu, K., 2017. "Programmable Deployment of Tensegrity Structures by Stimulus-Responsive Polymers". *Scientific Reports,* **7**(1), Dec., p. 1.

[11] Miriyev, A., Stack, K., and Lipson, H., 2017. "Soft material for soft actuators". *Nature Communications,* **8**(1), Sept., p. 596.

[12] Chautems, C., Tonazzini, A., Floreano, D., and Nelson, B. J., 2017. "A variable stiffness catheter controlled with an external magnetic field". In IEEE/RSJ International Conference on Intelligent Robots and Systems (IROS), pp. 181–186.

[13] Kovacs, G., Lochmatter, P., and Wissler, M., 2007. "An arm wrestling robot driven by dielectric elastomer actuators". *Smart Materials and Structures,* **16**(2), p. S306.

[14] Kwon Gu Han, Park Joong Yull, Kim Jeong Yoon, Frisk Megan L., Beebe David J., and Lee Sang-Hoon, 2008. "Biomimetic Soft Multifunctional Miniature Aquabots". *Small,* **4**(12), Nov., pp. 2148–2153.

[15] Shepherd, R. F., Ilievski, F., Choi, W., Morin, S. A., Stokes, A. A., Mazzeo, A. D., Chen, X., Wang, M., and Whitesides, G. M., 2011. "Multigait soft robot". *Proceedings of the National Academy of Sciences,* **108**(51), Dec., pp. 20400–20403.

[16] Song, Y. S., Sun, Y., Van Den Brand, R., Von Zitzewitz, J., Micera, S., Courtine, G., and Paik, J., 2013. "Soft robot for gait rehabilitation of spinalized rodents". In IEEE/RSJ International Conference on Intelligent Robots and Systems (IROS), pp. 971–976.

[17] Mosadegh, B., Polygerinos, P., Keplinger, C., Wennstedt, S., Shepherd, R. F., Gupta, U., Shim, J., Bertoldi, K., Walsh, C. J., and Whitesides, G. M., 2014.

"Pneumatic Networks for Soft Robotics that Actuate Rapidly". *Advanced Functional Materials,* **24**(15), Apr., pp. 2163–2170.

[18] Decroly, G., Mertens, B., Lambert, P., and Alain, D., 2020. "Design, characterization and optimization of a soft fluidic actuator for minimally invasive surgery". *International Journal of Computer Assisted Radiology and Surgery,* **15**, pp. 333–340.

[19] Overvelde, J. T. B., Kloek, T., D'haen, J. J. A., and Bertoldi, K., 2015. "Amplifying the response of soft actuators by harnessing snap-through instabilities". *Proceedings of the National Academy of Sciences,* **112**(35), Jan., pp. 10863–10868.

[20] Rus, D., and Tolley, M. T., 2015. "Design, fabrication and control of soft robots". *Nature,* **521**(7553), May, pp. 467–475.

[21] Hawkes, E. W., Christensen, D. L., and Okamura, A. M., 2016. "Design and implementation of a 300% strain soft artificial muscle". In 2016 IEEE International Conference on Robotics and Automation (ICRA), pp. 4022–4029.

[22] Yang, D., Verma, M. S., So, J.-H., Mosadegh, B., Keplinger, C., Lee, B., Khashai, F., Lossner, E., Suo, Z., and Whitesides, G. M., 2016. "Buckling Pneumatic Linear Actuators Inspired by Muscle". *Advanced Materials Technologies,* **1**(3), June, p. 1600055.

[23] Verrelst, B., Ham, R. V., Vanderborght, B., Daerden, F., Lefeber, D., and Vermeulen, J., 2005. "The Pneumatic Biped "Lucy" Actuated with Pleated Pneumatic Artificial Muscles". *Autonomous Robots,* **18**(2), Mar., pp. 201–213.

[24] De Greef, A., Lambert, P., and Delchambre, A., 2009. "Towards flexible medical instruments: Review of flexible fluidic actuators". *Precision Engineering,* **33**(4), Oct., pp. 311–321.

[25] Chou, C.-P., and Hannaford, B., 1996. "Measurement and modeling of McKibben pneumatic artificial muscles". *IEEE Transactions on Robotics and Automation,* **12**(1), Feb., pp. 90–102.

[26] Tondu, B., and Lopez, P., 2000. "Modeling and control of McKibben artificial muscle robot actuators". *IEEE Control Systems,* **20**(2), Apr., pp. 15–38.

[27] Tsagarakis, N., and Caldwell, D. G., 2000. "Improved modelling and assessment of pneumatic muscle actuators". In IEEE International Conference on Robotics and Automation (ICRA), Vol. 4, pp. 3641–3646.

[28] Krishnan, G., Bishop-Moser, J., Kim, C., and Kota, S., 2015. "Kinematics of a Generalized Class of Pneumatic Artificial Muscles". *ASME Journal of Mechanisms and Robotics,* **7**(4), Nov., p. 041014.

[29] Daerden, F., 1999. "Conception and realization of pleated pneumatic artificial muscles and their use as compliant actuation elements". PhD thesis, Vrije Universiteit Brussel.

[30] Ilievski, F., Mazzeo, A. D., Shepherd, R. F., Chen, X., and Whitesides, G. M., 2011. "Soft Robotics for Chemists". *Angewandte Chemie International Edition,* **50**(8), Feb., pp. 1890–1895.

[31] Calderón, A. A., Ugalde, J. C., Zagal, J. C., and Pérez-Arancibia, N. O., 2016. "Design, fabrication and control of a multi-material-multi-actuator soft robot inspired by burrowing worms". In IEEE International Conference on Robotics and Biomimetics (ROBIO), pp. 31–38.

[32] Gorissen, B., Vincentie, W., Al-Bender, F., Reynaerts, D., and Volder, M. D., 2013. "Modeling and bonding-free fabrication of flexible fluidic microactuators with a bending motion". *Journal of Micromechanics and Microengineering,* **23**(4), p. 045012.

[33] Bruyas, A., Geiskopf, F., Meylheuc, L., and Renaud, P., 2014. "Combining Multi-Material Rapid Prototyping and Pseudo-Rigid Body Modeling for a new compliant mechanism". In IEEE International Conference on Robotics and Automation (ICRA), pp. 3390–3396.

[34] Chen, Y., Le, S., Tan, Q. C., Lau, O., Wan, F., and Song, C., 2017. "A reconfigurable hybrid actuator with rigid and soft components". In IEEE International Conference on Robotics and Automation (ICRA), pp. 58–63.

[35] Comber, D. B., Slightam, J. E., Gervasi, V. R., Neimat, J. S., and Barth, E. J., 2016. "Design, Additive Manufacture, and Control of a Pneumatic MR-Compatible Needle Driver". *IEEE Transactions on Robotics,* **32**(1), Feb., pp. 138–149.

[36] Pfeil, A., Barbé, L., Wach, B., Bruyas, A., Geiskopf, F., Nierenberger, M., and Renaud, P., 2018. "A 3D-Printed Needle Driver Based on Auxetic Structure and Inchworm Kinematics". In ASME International Design Engineering Technical Conferences and Computers and Information in Engineering Conference (IDETC-CIE), p. V05AT07A057.

[37] Howell, L. L., 2001. *Compliant Mechanisms*. A Wiley-Interscience Publication. Wiley. OCLC: 247902557.

[38] Vos, R., and Barrett, R., 2011. "Mechanics of pressure-adaptive honeycomb and its application to wing morphing". *Smart Materials and Structures,* **20**(9), Sept., p. 094010.

[39] Pagitz, M., Lamacchia, E., and Hol, J. M. A. M., 2012. "Pressure-actuated cellular structures". *Bioinspiration & Biomimetics,* **7**(1), p. 016007.

[40] Martinez, R. V., Fish, C. R., Chen, X., and Whitesides, G. M., 2012. "Elastomeric Origami: Programmable Paper-Elastomer Composites as Pneumatic Actuators". *Advanced Functional Materials,* **22**(7), Apr., pp. 1376–1384.

[41] Li, S., and Wang, K. W., 2015. "Fluidic origami: A plant-inspired adaptive structure with shape morphing and stiffness tuning". *Smart Materials and Structures,* **24**(10), Oct., p. 105031.

[42] Schmitt, F., Piccin, O., Barbé, L., and Bayle, B., 2018. "Soft robots manufacturing: A review". *Frontiers in Robotics and AI,* **5**.

[43] Stratasys. Polyjet Process. https://www.stratasys.com/polyjet-technology.

[44] Weiss, L. E., Merz, R., Prinz, F. B., Neplotnik, G., Padmanabhan, P., Schultz, L., and Ramaswami, K., 1997. "Shape deposition manufacturing of heteroge-

neous structures". *Journal of Manufacturing Systems,* **16**(4), Jan., pp. 239–248.

[45] Bruyas, A., Geiskopf, F., and Renaud, P., 2015. "Design and Modeling of a Large Amplitude Compliant Revolute Joint: The Helical Shape Compliant Joint". *ASME Journal of Mechanical Design,* **137**(8), Aug., p. 085003.

[46] Schmitt, F., Piccin, O., Barbé, L., and Bayle, B., 2018. "An Origami-Inspired Flexible Pneumatic Actuator". In IEEE/RSJ International Conference on Intelligent Robots and Systems (IROS), pp. 436–441.

[47] Evans, K. E., 1991. "Auxetic polymers: A new range of materials". *Endeavour,* **15**(4), Jan., pp. 170–174.

[48] Karnessis, N., and Burriesci, G., 2013. "Uniaxial and buckling mechanical response of auxetic cellular tubes". *Smart Materials and Structures,* **22**(8), p. 084008.

[49] Azimian, H., Francis, P., Looi, T., and Drake, J., 2014. "Structurally-redesigned concentric-tube manipulators with improved stability". In IEEE/RSJ International Conference on Intelligent Robots and Systems (IROS), pp. 2030–2035.

[50] Mark, A. G., Palagi, S., Qiu, T., and Fischer, P., 2016. "Auxetic metamaterial simplifies soft robot design". In IEEE International Conference on Robotics and Automation (ICRA), pp. 4951–4956.

[51] Sedal, A., Fisher, M. W., Bishop-Moser, J., Wineman, A., and Kota, S., 2018. "Auxetic sleeves for soft actuators with kinematically varied surfaces". In IEEE/RSJ International Conference on Intelligent Robots and Systems (IROS), pp. 464–471.

[52] Gibson, L. J., Ashby, M. F., Schajer, G. S., and Robertson, C. I., 1982. "The mechanics of two-dimensional cellular materials". *Proceedings of the Royal Society of London. A. Mathematical and Physical Sciences,* **382**(1782), July, pp. 25–42.

[53] Bruyas, A., Geiskopf, F., and Renaud, P., 2015. "Toward unibody robotic structures with integrated functions using multimaterial additive manufacturing: Case study of an MRI-compatible interventional device". In IEEE/RSJ International Conference on Intelligent Robots and Systems (IROS), pp. 1744–1750.

[54] Pfeil, A., Barbé, L., Geiskopf, F., Gayral, T., Rubbert, L., and Renaud, P., 2019. Design tools for printed robots: Experience and ongoing work using multimaterial additive manufacturing. Workshop, IEEE International Conference on Robotics and Automation (ICRA).